Publications of the Astronomical Society of Australia (2026), **43**, e060, 15 pages
doi:10.1017/pasa.2026.10187

Research Article

Consistent gas-phase temperatures and metallicities from UV and optical nebular emission: A reliable foundation from $z = 0$ to cosmic dawn

Erin Huntzinger[1], Yuguang Chen[1,2], Tucker Jones[1], Ryan Sanders[3], Peter Senchyna[4], Daniel Stark[5], Fabio Bresolin[6], Stephane Charlot[7] and Jacopo Chevallard[8]

[1]Department of Physics and Astronomy, University of California Davis, USA, [2]Department of Physics, The Chinese University of Hong Kong, Hong Kong, [3]Department of Physics and Astronomy, University of Kentucky, USA, [4]Observatories of the Carnegie Institution of Washington, USA, [5]Department of Astronomy, University of California Berkeley, USA, [6]Institute for Astronomy, University of Hawai'i at Manoa, USA, [7]Sorbonne Universite, France and [8]Department of Physics, University of Oxford, UK

Abstract

The rest-frame ultraviolet (UV) spectra of star-forming galaxies are increasingly important as they become one of the primary windows to probe the physical properties of cosmic dawn ($z > 8$) galaxies with the James Webb Space Telescope. However, the systematic discrepancies between UV and optical gas-phase metallicity measurements remain poorly understood in the local universe, partly due to challenges in achieving precise comparisons between UV and optical spectra for the same objects. In this work, we introduce a novel method that leverages the He II λ1640 and He II λ4686 nebular emission lines to achieve accurate aperture and reddening corrections between UV and optical spectra. Here we apply this method to three nearby Blue Compact Dwarf (BCD) galaxies. Our results demonstrate that this approach enables precise measurements, with electron temperatures (T_e) derived from UV and optical spectra exhibiting closer agreement compared to previous studies, and O/H abundance agreeing within 0.1 dex. However, two BCDs appear to have lower UV-based electron temperatures $T_{e\,1666} < T_{e\,4363}$, in contrast to expectations from the temperature fluctuation model. We consider a variety of possible explanations for these unphysical temperatures – differential dust attenuation, aperture differences, and spatial extent of emission lines – but no suitable cause is identified. These findings suggest a complex gaseous environment associated with star formation, and underscore the need for additional observations to further investigate the nature of He II nebular emission and address the systematic issues between UV and optical nebular properties. Nonetheless, the close empirical agreement of these results indicates that UV- and optical-based nebular temperature and abundance measurements can be reliably compared within 0.1 dex, providing a solid foundation for evolutionary studies from the local Universe to cosmic dawn.

Keywords: Galaxies: abundances; galaxies: dwarf; ISM: abundances; HII regions; ultraviolet: ISM

(Received 29 January 2026; revised 5 March 2026; accepted 25 March 2026)

1. Introduction

The processes of gas accretion, star formation and gas outflows are paramount in understanding how galaxies form and evolve. Accurate measurements of gas-phase chemical composition provide some of the most robust constraints on these processes (e.g. Erb et al. 2006; Erb 2008; Peeples & Shankar 2011; Lilly et al. 2013; Davé, Finlator, & Oppenheimer 2011; Davé et al. 2017; Sanders et al. 2021). Gas accretion dilutes metals in the interstellar medium (ISM), star formation produces metals through nucleosynthesis and then returns them to the ISM through supernovae and stellar winds, and outflows remove metals from galaxies. Thus, the gas-phase metallicity of a galaxy is regulated by the interplay between gas inflows, outflows, and star formation. Consequently, studies of chemical evolution serve as a powerful tool to infer the baryonic processes shaping galaxies over cosmic time.

Gas-phase oxygen abundance (referred to herein as 'metallicity,' expressed as $12 + \log(\mathrm{O/H})$) has now been measured in galaxy populations reaching $z > 8$ with the James Webb Space Telescope (JWST; e.g. Arellano-Córdova et al. 2022; Schaerer et al. 2022; Taylor, Barger, & Cowie 2022; Bunker et al. 2023; Curti et al. 2023; Nakajima et al. 2023; Sanders et al. 2023; Trump et al. 2023; Sarkar et al. 2025). These advancements build upon extensive earlier surveys that have mapped metallicity evolution across $z \simeq 0$–4 (e.g. Kriek et al. 2015; Steidel et al. 2014; Wisnioski et al. 2015; Stott et al. 2016; Treu et al. 2015; Momcheva et al. 2016). These efforts have consistently found lower metallicities at higher redshifts and at lower stellar masses (e.g. Tacconi et al. 2018; Sanders et al. 2021; Tremonti et al. 2004; Cullen et al. 2014; Curti et al. 2020; Troncoso et al. 2014; Andrews & Martini 2013; Erb et al. 2006; Maiolino et al. 2008). The observed mass-metallicity relation and its evolution are primarily attributed to a mass-dependent outflow rate, and higher gas fractions at earlier cosmic epochs.

Corresponding author: Yuguang Chen; Email: yuguangchen@cuhk.edu.hk

Cite this article: Huntzinger E, Chen Y, Jones T, Sanders R, Senchyna P, Stark D, Bresolin F, Charlot S and Chevallard J. (2026) Consistent gas-phase temperatures and metallicities from UV and optical nebular emission: A reliable foundation from $z = 0$ to cosmic dawn. *Publications of the Astronomical Society of Australia* **43**, e060, 1–15. https://doi.org/10.1017/pasa.2026.10187

The most common approach to measuring the O/H abundances relies on nebular emission lines originating in H II regions. Collisionally excited lines (CELs) from [O III] are particularly sensitive to the electron temperature (T_e). The T_e can be determined from the ratio of two CELs probing different upper energy levels (e.g. [O III] λ4363/[O III] λ5007) and used to calculate the emissivity of oxygen and other emission lines, allowing for a precise determination of O/H abundance. This technique, known as the 'direct T_e' method, is commonly applied to rest-frame optical observations. However, recent JWST observations of galaxies at $z \gtrsim 8$ increasingly rely on rest-UV nebular emission lines (e.g. O III] λλ 1661, 1666, C III] λλ1907, 1909, C IV λλ1549, 1551) to probe gas-phase properties (e.g. Curti et al. 2025; Hayes et al. 2025; Hsiao et al. 2025; Tang et al. 2025; Arellano-Córdova et al. 2026), as the optical lines are redshifted into the more observationally challenging mid-infrared, particularly observations at $z \gtrsim 10$. Compared to the extensive optical surveys, rest-UV spectroscopic datasets at low redshift remain more limited due to atmospheric opacity below ∼ 3000 Å and the necessary reliance on space-based facilities with limited sensitivity. Recent programmes with the Hubble Space Telescope such as the COS Legacy Archive Spectroscopic SurveY (CLASSY; Berg et al. 2022; James et al. 2022) have substantially improved the availability of high-quality UV spectra for nearby star-forming galaxies, enabling the development of UV-based nebular diagnostics and providing insights into the ionising stellar populations that shape UV line ratios. However, precise and widely calibrated T_e measurements based on UV collisionally excited lines remain comparatively scarce relative to their optical counterparts.

Another challenge for chemical evolution studies is that even in sensitive rest-optical spectra, two 'direct' methods which can be used to derive the O^{++}/H^{+} nebular abundance in an H II region systematically disagree. O/H abundances from CELs using the direct-T_e method are found to be systematically lower (by ∼0.2–0.3 dex) compared to measurements from the much fainter oxygen recombination lines (RLs). This so-called abundance discrepancy factor (ADF; e.g. Tsamis et al. 2003; Blanc et al. 2015; Esteban et al. 2009; Esteban et al. 2014; García-Rojas et al. 2004; García-Rojas & Esteban 2007) is often attributed to temperature fluctuations of the gas within H II regions (Peimbert 1967; García-Rojas et al. 2004). In this scenario, T_e values measured from optical CELs are biased high resulting in the direct-T_e metallicities biased low. Meanwhile, the recombination line metallicities are accurate due to their insensitivity to T_e. For the UV emission lines, such as O III] λλ 1661, 1666, this would suggest that T_e derived from rest-UV lines would be biased even higher and thus metallicities even lower compared to the optical CELs. On the other hand, another explanation of the ADF involves inclusions of high-metallicity gas (Croxall et al. 2013; Stasińska et al. 2007) among an ambient medium with lower metallicity, in which case the CELs are expected to be more accurate than RLs. Some studies have found good agreement between the metallicities of young stars and CEL-based nebular measurements (e.g. Bresolin et al. 2016; Bresolin et al. 2025), suggesting that T_e metallicities may be more reliable. As the cause of the ADF is currently not conclusively established, empirical relationships are important to establish the relative biases between different metallicity measurement techniques, such as the joint use of UV and optical CELs.

Significant efforts have been made in recent years to understand the gas properties measured from UV nebular emission in the local universe (e.g. Kunth et al. 1997; Senchyna et al. 2017; Senchyna et al. 2020; Senchyna et al. 2022; Berg et al. 2022; Kelly et al. 2025). However, measuring the T_e and metallicity using UV emission lines is challenging, since it requires an accurate comparison between the UV and optical fluxes (e.g. C III] λλ1907, 1909 and H I Balmer lines or using O III] λ1666/[O III] λ5007 to derive T_e.). Such comparisons often introduce systematic uncertainty from different instruments and apertures used for the UV and optical measurements (e.g. Arellano-Córdova et al. 2022), in addition to highly uncertain reddening corrections. Using the CLASSY survey, Mingozzi et al. (2022) explored the promise and limitations of combining Hubble Space Telescope (HST)/Cosmic Origins Spectrograph (COS) UV spectra and various optical spectra by matching the continuum spectra to the stellar population synthesis models. Their results suggest that the [O III] T_e measured from the UV emission (via O III] λλ 1661, 1666/[O III] λ5007) is consistent with the optical T_e (via [O III] λ4363/[O III] λ5007) on average with a sample standard deviation scatter of ∼1500 K (∼10% of T_e), in relatively good agreement, but with substantial uncertainties related to dust attenuation and other effects.

In this work, we demonstrate a novel method to achieve precise comparison between the optical and UV fluxes. A key goal is to minimise uncertainty associated with combining UV and optical features, including aperture corrections and dust attenuation. We achieve this using nebular He II emission lines, namely UV He II λ1640 and optical He II λ4686. While the ionisation source of these emission lines in H II regions is still under debate (Kehrig et al. 2011; Kehrig et al. 2015; Schaerer, Fragos, & Izotov 2019; Senchyna et al. 2020), the production mechanism of nebular He II emission is believed to be dominated by recombination processes (Schaerer & Vacca 1998) analogous to the H I Balmer and Paschen lines. Accordingly, the flux ratio He II λ1640/He II λ4686 ≈ 6.99 is expected to be nearly constant and relatively insensitive to gas density and T_e. This provides a valuable reference to calibrate observed fluxes from different instruments at rest-frame UV and optical wavelengths. In this work, we demonstrate that this method can provide precise measurements of T_e and metallicity, and examine whether gas properties measured from UV features are systematically different from equivalent optical diagnostics.

This paper is organised as follows. We present target galaxy selection and observations in Section 2. Section 3 describes our methodology and analysis, including flux calibration of optical and UV spectra, dust attenuation and aperture corrections, and measurements of the physical properties. We discuss the reliability of our measurements and the physical implications in Section 4. Section 5 summarises our results. Emission line analyses (including correction for dust attenuation and determination of the physical properties of the gas) are performed using PYNEB (Luridiana, Morisset, & Shaw 2015). We adopt the collision strengths from Tayal & Zatsarinny (2017) for the O^{++} ion and the transition probabilities for all relevant lines from Froese Fischer & Tachiev (2004) throughout this work.

2. Sample selection and data

Here, we describe the target sample and spectroscopic data used in this work. Our sample was selected from a superset of ten metal-poor star-forming galaxies analysed in (Senchyna et al. 2017, hereafter S17), which presented UV spectra of these galaxies from HST's Cosmic Origins Spectrograph (COS) along with optical spectra from Keck's Echelle Spectrograph and Imager (ESI;

Table 1. Summary of target galaxy properties.

Object:	SB 2[a]	SB 82	SB 182
Alternative ID:	J0944-0038, CGCG007-025	MRK 193	J1148+2546, LEDA 36857
RA	9:44:01.87	11:55:28.34	11:48:27.34
DEC	−0:38:32.2	57:39:52.0	25:46:11.8
$z_{\rm UV}$[b]	0.00486	0.01726	0.04515
$\log(M_*/M_\odot)$[c]	5.1	6.4	7.3
$\log({\rm SFR}/(M_\odot\ {\rm yr}^{-1}))$[d]	$-1.49\pm^{0.21}_{0.15}$	–	$+0.29\pm^{0.18}_{0.15}$
12+log(O/H)[c]	7.81 ± 0.07	7.91 ± 0.04	8.01 ± 0.04
r_{50}[d]	0.984	–	0.874
n_e (cm^{-3})[e]	158	189	184

[a] Values for SB 2 reflect the brightest star-forming region in the central knot of the galaxy, as opposed to the (larger) entire galaxy.
[b] Redshifts measured from O III] λλ 1661, 1666 nebular emission lines.
[c] Obtained from Senchyna et al. (2017). M_* was measured from SED fitting with a typical uncertainty of 0.1 dex, and $12 + \log({\rm O/H})$ was measured using the optical direct T_e method.
[d] Obtained from Berg et al. (2022), where SFR was measured using Beagle SED fitting.
[e] n_e derived from the [S II] λλ6731/6716 flux ratio for each object.

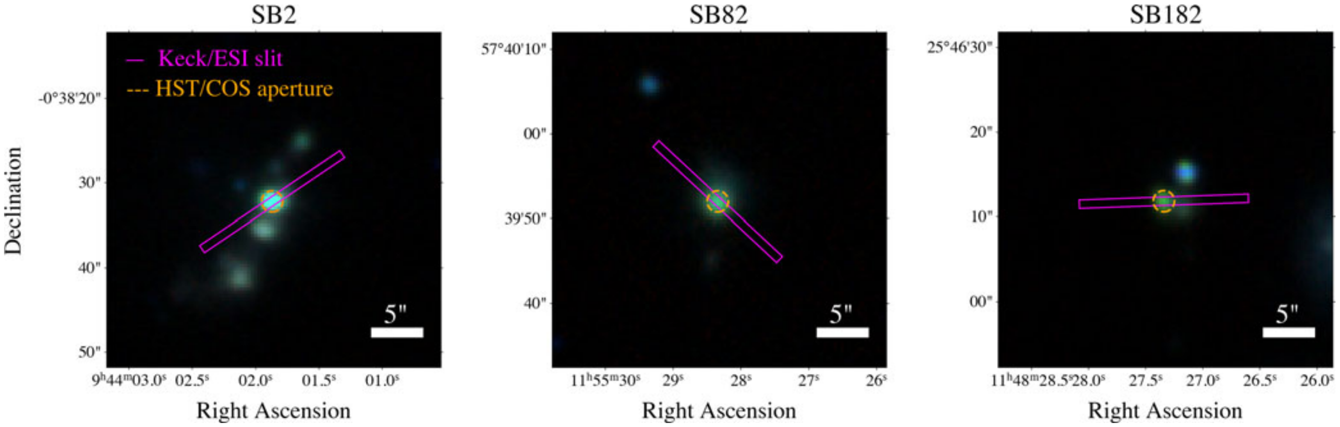

Figure 1. Images of the three blue compact dwarf galaxies studied in this work. Each panel shows a SDSS *u, g, r* false-colour image, the *HST/ COS* 2″5 aperture (circles), and the Keck/ ESI 1 × 20 slit (rectangles). The 25 COS aperture size corresponds to projected diameters of 0.23 kpc for SB 2, 0.92 kpc for SB 82, and 2.31 kpc for SB 182 (Senchyna et al. 2017). Near-UV target acquisition images from COS for all three objects can be found in S17. All three objects are dwarf galaxies containing one primary H II region, from which the majority of nebular line emission is captured by both the COS and ESI apertures.

Sheinis et al. 2002). These galaxies were initially selected based on the presence of prominent He II λ4686 emission in their optical SDSS spectra (Shirazi & Brinchmann 2012). Since our objective is to characterise UV and optical nebular emisson, we restrict our analysis to the sample of galaxies exhibiting clear narrow nebular He II λ1640 and He II λ4686 emission (as opposed to broad stellar wind emission) in high-resolution HST/COS and Keck/ESI spectra. The combination of optical and UV He II lines is necessary to obtain precise dust reddening and aperture corrections (see Section 3.2.2 for details).

The He II selection criteria result in a sample of three blue compact dwarf galaxies (BCDs) with relatively low metallicities ($12+\log({\rm O/H}) < 8.1$) and recent star formation activity. The properties of these galaxies are summarised in Table 1. Figure 1 presents optical images of the three BCDs. Below, we briefly outline the physical characteristics of each target (masses from S17):

- **SB 2** is a dwarf galaxy hosting multiple star-forming regions. Our analysis centres on the brightest star-forming region located in the central knot, as shown in Figure 1, which has a stellar mass of $M_* = 10^{5.1}$ M$_\odot$. This region was captured in isolation within the COS aperture (Senchyna et al. 2022, hereafter S22). The values used in this work pertain exclusively to the region enclosed by the COS aperture and do not account for the contributions from neighbouring star-forming regions in the galaxy.
- **SB 82** is an isolated dwarf galaxy with a stellar mass of $M_* = 10^{6.4}$ M$_\odot$, also known as Mrk 193.
- **SB 182** is a dwarf galaxy with a stellar mass of $M_* = 10^{7.3}$ M$_\odot$. Morphologically, it consists of two distinct components separated by several arcseconds. In this study, we focus on the southeast star-forming region. The angular separation between the two components is sufficient to ensure that the northwest component was not included in the spectra analysed here.

2.1. Keck/ESI

The ESI data were taken on 29 March 2016 (SB 82) and 20 January 2017 (SB 2 and SB 182). Sky conditions were clear with 0.8–1.2 arcsec seeing. The 1” slit width was used, resulting in spectral resolution $R \sim 4\,000$ (75 km s^{-1} FWHM) spanning 3 900–10 900 Å. To minimise aperture loss due to atmospheric dispersion, all observations were taken with a slit position near the parallactic angle (PA $= 304$ for SB 2, 227 for SB 82, and 272 for SB 182). The total integration time was 2 h for SB 2 and 2.5 h for SB 82 and SB 182, split into individual exposures of 30 min each. The spectra were reduced using the ESIREDUX data reduction pipeline as described in S17.

To improve flux calibration relative to the ESIREDUX processing, we scale the continuum level of Keck/ESI spectra to match that in the fully calibrated spectra available for each target from the Sloan Digital Sky Survey (SDSS; York et al. 2000). We first masked out wavelength regions around the strong emission lines, and then excluded pixels deviating more than 2σ from the running median in bins of 50 Å to mask detected spectral features. The masking of weak lines was necessary to robustly estimate the continuum due to the large number of emission lines detected (>100 per target) in these sensitive spectra. We then fit a univariate cubic spline to the masked spectrum to obtain a smooth model of the continuum in the ESI spectrum. We performed the same steps on the SDSS spectrum, and divide the ESI by SDSS continuum model to obtain the flux calibration scaling factor. We then scale the ESI flux and error spectra by this factor. Figure 2 shows the flux-calibrated ESI spectra of the three objects in the wavelength ranges most relevant for this work.

2.2. HST/COS

The HST/COS spectroscopic observations for the BCDs have been previously presented in S17 and S22. Here we give a brief summary. The spectra were obtained using the 2″5 COS aperture with the G160M grating centred at 1 533 Å. For SB 2 and SB 82, the COS data were taken on 4–5 April 2020 (SB 2) and 21 November 2019 (SB 82) as part of the Cycle 26 HST-GO-15646 programme. For SB 182, the data were taken on 05 November 2015 as part of the Cycle 23 HST-GO-14168 programme. The total exposure times were 26 925.12 s for SB 2, 29 255.52 s for SB 82, and 2 624.61 s for SB 182. The spectral resolution of the COS data is $\sim 15\,000$. Data for all three targets were reduced using the standard Calcos pipeline,[a] with the calibration files downloaded from the Space Telescope Science Data Analysis System (STSDAS).[b] For spectral extraction, we employed the 'TWOZONE' algorithm. Additional details on data reduction and extraction for all three targets are provided in S17 and S22.

3. Analysis

The objectives of this work require computing the O^{++} abundance from the optical [O III] λ4959/Hβ ratio using T_e measured from the UV O III] λ1666/[O III] λ4959 emission line ratio, and comparing it with T_e derived from the optical [O III] λλ4363/4959 ratio. This approach requires measuring accurate line fluxes from both the UV and optical spectra. Given the different excitation energies, O III] λλ1661,1666 is more sensitive to T_e than [O III] λ4363. Comparing these measurements can therefore provide constraints on temperature fluctuations within the ionised gas, which should cause the UV-based T_e to to be biased higher than the T_e derived from optical [O III] λ4363. In this section we provide a detailed description of these measurements and methodology.

3.1. Emission line fluxes

3.1.1. Optical line fitting

While a large number of emission lines are detected in the Keck/ESI spectra, our analysis requires only a modest subset detected at very high signal-to-noise ratios: the H I Balmer and Paschen series, [O III] λ4363, [O III] λ4959, He II λ4686, and the density-sensitive [S II] λ6716, 6731. We measured line fluxes by fitting Gaussian profiles superposed on a linear continuum. He II λ4686 can have a broad component from winds of massive stars as well as a narrow nebular component, of which only the nebular component is of interest to this analysis. We thus include both a broad and narrow Gaussian component when fitting He II λ4686, but only report fluxes for the narrow nebular component. SB 2 and SB 182 display no broad component in the ESI spectra. SB 82 shows weak but detected broad He II λ4686 emission, with the peak flux density of the broad component $\approx 5\times$ smaller than the narrow peak flux density. Visual inspection of the best fits indicates that the two-Gaussian model adequately matches the observed He II λ4686 profile in SB 82 and reliably recovers the flux of the narrow component. Table 2 gives the observed optical line fluxes relative to Hβ, in units where I(Hβ) $= 100$. We show best-fit profiles to the most relevant features (namely [O III] λ4363, He II λ4686, Hβ, and [O III] λ4959) in Figure 3.

We do not use the Hα or [O III] λ5007 lines because their peaks are nonlinear or saturated in the ESI spectra. Including these lines would not significantly affect the results, as equivalent information is obtained from [O III] λ4959 and numerous H I lines (most importantly Hβ and Hγ). We have confirmed that the optical line fluxes used in this analysis are consistent between the SDSS and ESI spectra. In this work we use the ESI data which has significantly higher signal-to-noise and spectral resolution.

3.1.2. UV line fitting

The He II λ1640, O III] λ1661, and O III] λ1666 UV emission lines were originally described in S17, based on HST/COS spectra with limited exposure times (one orbit) for all three objects. Subsequent observations with significantly longer exposure times were obtained for SB2 and SB82, reported in S22. In this work we refit the UV line fluxes using the deeper spectra from these new observations. All three lines were fit using a Gaussian profile plus a linear continuum. Milky Way interstellar absorption features were masked out where necessary. The O III] λ1666 and O III] λ1661 lines originate from the same upper energy level, resulting in a fixed O III] λ1666/O III] λ1661 flux ratio that is independent of T_e and n_e. Thus, we performed a joint fit to O III] λλ1661, 1666 with the same width and redshift for both lines, and fixing the flux ratio to the theoretically expected value of 2.49 which we calculated using PYNEB (Luridiana et al. 2015).

The He II λ1640 emission was fit independently from the O III] λλ1661, 1666 doublet. The redshifts measured from He II and O III] are consistent with one another for each object. While SB 82 exhibits a broad component of optical He II λ4686, we do not detect significant broad He II λ1640 emission. Given the flux ratio between the broad and narrow components of the optical He II λ4686 emission, we indeed do not expect to detect the broad component in the He II λ1640 observations (see Section 3.1.1 and

[a] CALCOS documentation.
[b] STSDAS documentation.

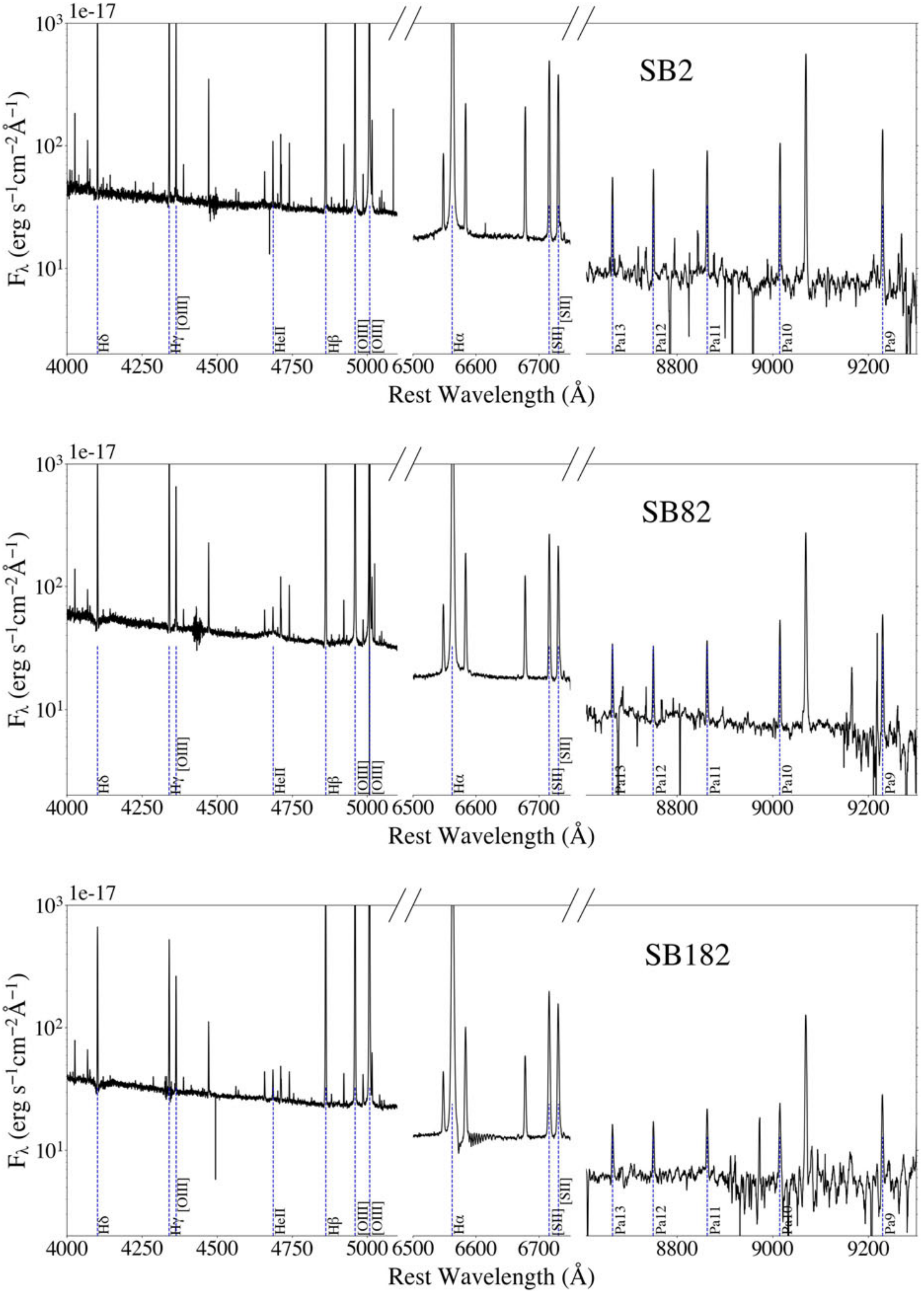

Figure 2. Keck/ESI optical spectra of the three objects presented in this work. Prominent emission features, epecially the ones useful for this work, are labeled and marked with vertical dashed lines. All relevant features are clearly detected, including nebular He II λ4686. A broad He II component is visible in SB 82.

Table 2. Observed and de-reddened fluxes in units of I (Hβ) = 100.

Object:	SB 2		SB 82		SB 182	
Transition	Uncorrected	Corrected	Uncorrected	Corrected	Uncorrected	Corrected
Optical (Keck/ESI):						
Hδ	24.1 ± 0.3	27.3 ± 1.1	24.3 ± 0.3	24.7 ± 1.1	26.3 ± 0.3	26.3 ± 0.8
Hγ[a]	44.2 ± 1.0	48.2 ± 2.2	45.7 ± 0.8	46.3 ± 2.2	–	–
[O III] λ4363	11.8 ± 0.1	12.8 ± 0.5	12.8 ± 0.1	13.0 ± 0.6	10.2 ± 0.1	10.2 ± 0.3
He II λ4686	1.09 ± 0.04	1.12 ± 0.06	0.661 ± 0.022	0.664 ± 0.037	0.972 ± 0.027	0.972 ± 0.038
Hβ	100.0 ± 1.7	100.0 ± 4.3	100.0 ± 1.4	100.0 ± 4.7	100.0 ± 1.5	100.0 ± 3.1
[OIII]λ4959	187.0 ± 3.0	185.0 ± 8.0	229.0 ± 3.0	228.0 ± 11.0	213.0 ± 2.0	213.0 ± 6.0
[S II] λ6716	9.38 ± 0.15	7.86 ± 0.33	8.27 ± 0.09	8.05 ± 0.37	11.6 ± 0.2	11.6 ± 0.4
[S II] λ6731	7.19 ± 0.08	6.02 ± 0.24	6.44 ± 0.04	6.27 ± 0.28	8.99 ± 0.09	8.98 ± 0.26
P12	1.34 ± 0.02	0.980 ± 0.040	1.08 ± 0.02	1.02 ± 0.05	0.950 ± 0.016	0.948 ± 0.031
P11	2.06 ± 0.04	1.49 ± 0.06	1.26 ± 0.02	1.20 ± 0.06	1.33 ± 0.02	1.33 ± 0.04
P10	2.50 ± 0.04	1.80 ± 0.08	1.97 ± 0.02	1.87 ± 0.09	1.74 ± 0.08	1.74 ± 0.10
P9	3.39 ± 0.07	2.42 ± 0.11	2.53 ± 0.05	2.40 ± 0.12	2.20 ± 0.04	2.19 ± 0.07
$E(B-V)$:	0.167 ± 0.017		0.035 ± 0.016		0.001 ± 0.012	
Hβ flux[c]:	9 007.0 ± 47.0		5 933.0 ± 46.0		3 453.0 ± 25.0	
UV reddening and aperture uncorrected and corrected lines (HST/COS):						
He II λ1640	1.30 ± 0.04	7.77 ± 0.54	1.26 ± 0.08	4.50 ± 0.61	1.58 ± 0.23	6.75 ± 1.53
O III]λ1661[b]	1.13 ± 0.02	6.77 ± 1.35	2.29 ± 0.03	8.14 ± 0.99	0.95 ± 0.08	4.06 ± 0.78
O III] λ1666[b]	2.81 ± 0.05	18.6 ± 1.97	5.70 ± 0.07	20.3 ± 2.5	2.37 ± 0.21	10.1 ± 1.9

[a] Hγ in SB 182 is affected by a detector artifact, and was not used for optical reddening correction in this object.

[b] From a joint fit of O III] $\lambda\lambda$1661, 1666.

[c] The observed Hβ fluxes before extinction correction (units: $10^{-17}\,\mathrm{erg\,s^{-1}\,cm^{-2}\,Å^{-1}}$).

Figures 2, 3). Likewise we do not detect broad He II λ1640 in SB 2 and SB 182. Consequently we fit the UV He II λ1640 lines with a single narrow component, which provides an adequate fit to the data. The resulting nebular emission fluxes are reported in Table 2, and lines fits are shown in Figure 4.

3.2. Dust and aperture corrections

Accurately measuring metallicities from UV emission lines requires reliable comparisons between the UV and optical fluxes. A key objective of this work is to evaluate the effectiveness of using He II recombination lines for dust and aperture corrections. In this section, we outline the methodology to perform these corrections.

3.2.1. Optical reddening correction

Before applying the dust and aperture corrections between the optical and UV, we first corrected the optical line flux ratios for dust attenuation. This correction was performed using the standard nebular reddening correction method based on H II Balmer and Paschen line ratios. First, multiple $E(B-V)$ values were calculated using the ratios of Hγ, Hδ, and the 8 750.47, 8 862.79, 9 014.91 and 9 229.01 Å Paschen lines (P12, P11, P10, P9) relative to Hβ. Our fiducial analysis assumes the Cardelli et al. (1989) extinction law with $R_V = 3.1$, while alternative extinction laws and R_V values are discussed below in this section. Intrinsic flux ratios relative to Hβ were calculated in PyNeb assuming an electron temperature $T_e =$ 15 000 K and an electron density $n_e =$ 175 cm-3, corresponding to typical values in our sample (Section 3.3). The final $E(B-V)$ value was then calculated as the inverse-variance weighted mean of the individual $E(B-V)$ estimates. Hα was not used due to saturation. The dust corrected optical fluxes normalised to I (Hβ) = 100 are listed in Table 2. While we report fluxes normalised to Hβ as is standard practice, He II λ4686 is the most relevant reference point for the joint analysis of optical and UV lines.

In order to account for systematic uncertainties arising from optical dust attenuation correction, we considered several extinction laws prior to choosing the well-established Cardelli et al. (1989) curve for our analysis. Additionally, we use a range of H-Balmer and Paschen lines for the correction, which cover the spectral range of ∼4 100–9 200 Å. The relative reddening correction between [O III] λ4959 and [O III] λ4363, which both fall well within the range covered by the hydrogen lines, should not be sensitive to the choice of reddening curve. We tested three curves (Cardelli et al. 1989; Calzetti et al. 2000; Gordon et al. 2003) with varying $R_v = 3.1$–4.1. The change in the [O III] λ4363/[O III] λ4959 ratio is within 0.7% of our fiducial choice.

3.2.2. UV reddening and aperture correction

Dust attenuation laws exhibit significant variation in the ultraviolet (e.g. Cardelli et al. 1989; Calzetti et al. 2000; Gordon et al. 2003), introducing substantial systematic uncertainties in UV-to-optical line ratios (e.g. O III] λ1666/[O III] λ4959). Furthermore, differences in the acquisition apertures and point-spread functions between the Keck/ESI and HST/COS spectra complicate direct comparisons. By leveraging the UV He II λ1640 and optical He II λ4686 recombination lines, both issues are simultaneously addressed.

The intrinsic flux ratio He II λ1640/He II λ4686 = 6.99 (He II λ4686/He II λ1640 = 0.143) at $T_e = 15\,000$ K and $n_e = 175$ cm^{-3},

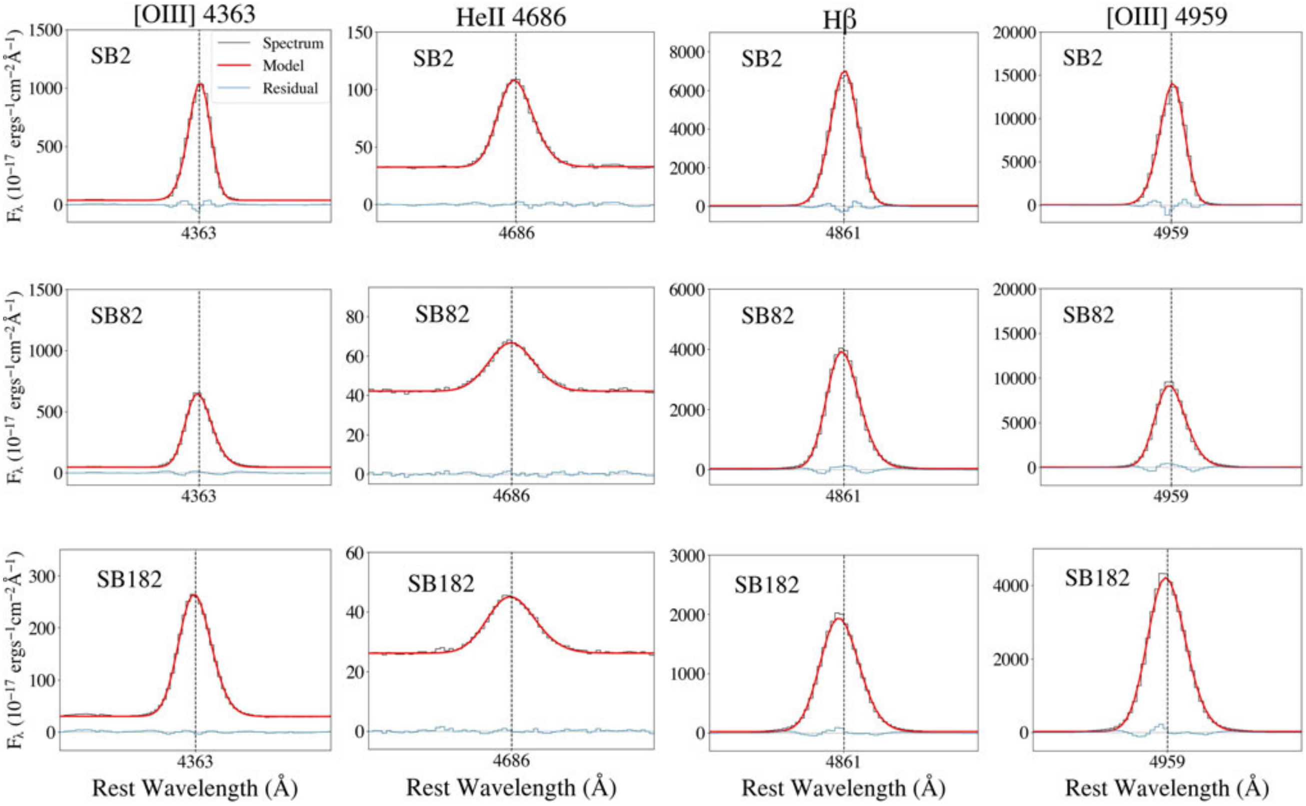

Figure 3. Rest-frame Keck/ESI spectra with the best-fit Gaussian profile and residual for select emission lines used in this analysis for each target. The *x*-axis range is 10 Å for all spectra presented in this figure and the *y*-axis is at a scale of 10^{-17} erg s^{-1} cm^{-2} Å^{-1}. We adopt a double Gaussian profile for He II λ4686 in SB 82, representing both the broad stellar and narrow nebular components. The broad component spans $\gtrsim$ 100 Å so it is not shown at the scale of this figure, but can be seen in Figure 2. All other lines are adequately fit with a single narrow component.

and is relatively insensitive to variations in T_e and n_e over the range of temperatures we investigate, making this ratio a reliable tool for correcting dust reddening between UV and optical nebular lines. This approach is similar to the use of H I line ratios in correcting optical attenuation. (We note that while the He II λ4686/He II λ1640 ratio is relatively stable, it is more affected by T_e than H I. We address this concern later in this section.) After the optical lines have been corrected for dust reddening (as described in Section 3.2.1), the reddening-corrected and aperture-matched He II λ1640 flux can be determined by comparing the observed He II λ4686/He II λ1640 flux ratio to its intrinsic value. The correction factor f_c can be expressed as

$$f_c = \left(\frac{\text{He II 4686}_{\text{corr}}}{\text{He II 1640}_{\text{unc}}}\right)_{\text{obs}} \times \left(\frac{\text{He II 1640}}{\text{He II 4686}}\right)_{\text{int}}, \qquad (1)$$

where He II λ4686_{corr} is the dust-corrected He II λ4686 flux, He II λ1640_{unc} is the uncorrected observed He II λ1640 flux, and (He II λ1640/He II λ4686)$_{\text{int}}$ is the intrinsic flux ratio between the two lines.

Once this correction factor is determined, it can be applied to the O III] λ1666 and O III] λ1661 lines. Since the O III] λ1666, O III] λ1661 doublet and He II λ1640 are relatively close in wavelength, the variation in the correction factor between these lines is minimal. For the Cardelli et al. (1989) extinction curve with $R_V = 3.1$ and $E(B-V) = 0.167$ (the maximum $E(B-V)$ value among the three objects), the correction factor changes by only 0.5% between O III] λ1666 and He II λ1640. For the Calzetti et al. (2000) curve with $R_V = 3.1$, the difference in correction factor is only 1% and for the Gordon et al. (2003) curve with $R_V = 3.41$ (2.74), the difference is only 0.2% (0.15%). This difference is well within the uncertainties of our analysis, regardless of the chosen attenuation curve. Thus, we apply the He II-based correction factor to the UV O III] λλ1661, 1666 emission lines via

$$F_{\lambda i\,(corr)} = F_{\lambda i\,(\text{unc})} \times f_c, \qquad (2)$$

where $F_{\lambda i\,(\text{corr})}$ and $F_{\lambda i\,(\text{unc})}$ are then the corrected and uncorrected fluxes for transition i, respectively. The corrected UV line fluxes are reported in units of I(Hβ) = 100 in Table 2.

While the intrinsic He II λ4686/He II λ1640 flux ratio is relatively stable, it does exhibit a slight dependence on T_e, which could introduce systematic biases into our analysis. The relationship between T_e in different ionic gas regions, including between He^+ and O^{++} zones, remains an active topic of investigation (e.g. Esteban et al. 2014; Kreckel et al. 2022; Rickards Vaught et al. 2024). Furthermore, nebular zones with different degrees of ionisation may be correlated with different levels of temperature fluctuations (Méndez-Delgado et al. 2022). To account for this, we incorporate a systematic uncertainty of ±4 000 K in the He II T_e when deriving the correction factor. This choice is motivated by the typical T_e differences observed between low-ionisation (e.g. [O II]) and high-ionisation (e.g. [O III]) zones in low-metallicity, high-ionisation H II regions (e.g. Rickards Vaught et al. 2024). This uncertainty is added in quadrature to the UV emission line flux measurement uncertainties. The weight

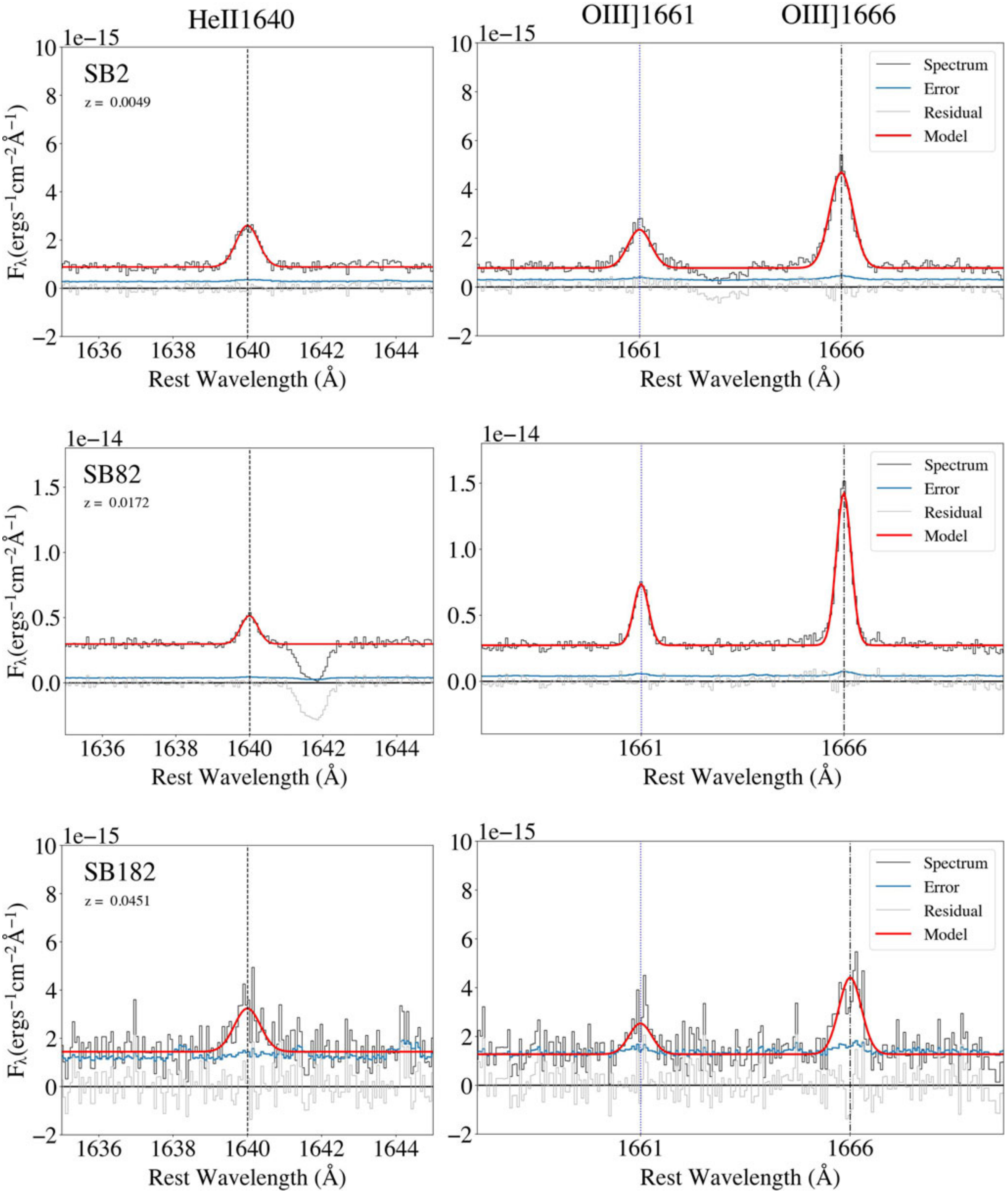

Figure 4. Binned HST/COS spectra, associated 1σ error spectra, best-fit Gaussian models, and residual spectra for our targets SB 2, SB 82 and SB 182. SB 2 and SB 82 have 10 orbits of COS data (Senchyna et al. 2022), while SB 182 has only a single orbit (Senchyna et al. 2017). Above, z is the redshift as measured from the observed UV spectra. f_{1640}, f_{1661} and f_{1666} are the measured flux and 1σ uncertainty for He II λ1640, O III] λ1661 and O III] λ1666, respectively. Milky Way interstellar absorption features (e.g. at rest wavelengths of approximately 1 663 Å for SB 2 and 1 642 Å for SB 82) were masked and excluded from the fitting. All emission lines used in our analysis are well-detected and unaffected by Milky Way absorption.

Table 3. Measured T_e, T_0, and t^2 values for SB 82, SB 182, and SB 2. We note that variances $t^2 < 0$ are formally unphysical.

Object	n_e (cm^{-3})	$T_{e\,4363}$ (K)	$T_{e\,1666}$ (K)	T_0 (K)	t^2
SB2	158	16 410.0 ± 502.0	15 703.0 ± 324.0	17 672.0 ± 909.0	−0.054 ± 0.043
SB82	189	14 971.0 ± 373.0	15 257.0 ± 365.0	14 235.0 ± 950.0	0.024 ± 0.033
SB182	184	13 869.0 ± 259.0	12 986.0 ± 536.0	15 779.0 ± 702.0	−0.078 ± 0.031

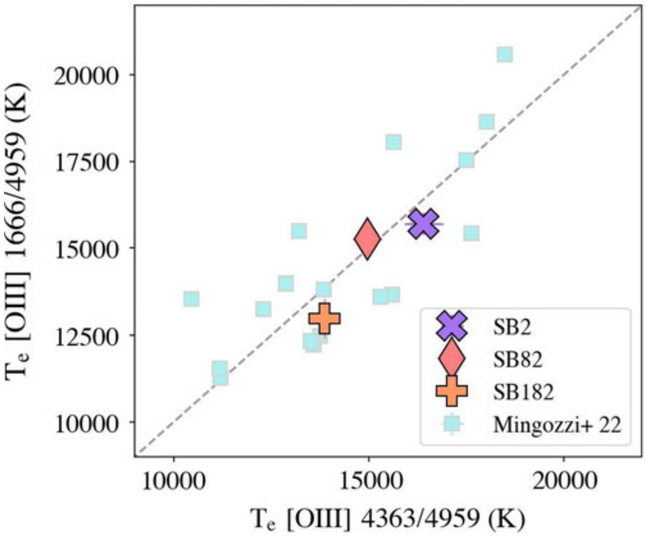

Figure 5. Our measurements of $T_{e\,1666}$ versus $T_{e\,4363}$ for the objects in our sample, along with measurements from Mingozzi et al. (2022) which used a different methodology. Two galaxies in our sample (SB 2 and SB 182) have $T_{e\,1666} + < +T_{e\,4363}$, whereas temperature fluctuations predict the opposite result. Our sample displays a tight distribution with standard deviation scatter of 515 K (4.2% mean absolute percent offset), while the Mingozzi et al. (2022) sample has a larger scatter of 1557 K (9.2% mean absolute percent offset). The improved precision demonstrates success in reducing the uncertainties associated with UV attenuation corrections using our He II method (see Section 3.2.2).

that this uncertainty carries in our final results varies by object. Error on the quantification of temperature fluctuations in our final results (see Section 4.1: *Temperature Fluctuations*) for SB 2 and SB 182 is not substantially affected by the uncertainty introduced by the intrinsic He II λ4686/He II λ1640 ratio because uncertainty from flux measurements dominates. However, for SB 82, the error introduced by the temperature dependence of the correction factor is co-dominant with the UV flux error (i.e. signal-to-noise) and accounts for approximately 30% of the t^2 error budget.

3.3. Measurement of O^{++} electron temperature

To measure the O^{++} abundance, the electron temperature (T_e) of the ionised gas must first be determined in order to calculate the emissivity of the [O III] emission lines. The T_e can be derived from the ratio of collisionally excited lines originating from different upper energy levels (e.g. Osterbrock & Ferland 2006). In this work we obtain two measurements of T_e for each object using the dust-corrected flux ratios [O III] λλ4363/4959 and O III] λ1666/[O III] λ4959, hereafter referred to as $T_{e\,4363}$ and $T_{e\,1666}$, respectively. The $^1D_2 \rightarrow ^3 P_1$ energy level transition produces the [O III] λ4959 emission line, $^1S_0 \rightarrow ^1 D_2$ produces [O III] λ4363, and $^5S_2^o \rightarrow ^1 D_2$ produces O III] λ1666. Each transition samples a different upper energy level for the O^{++} ion, which consequently sample different collisional energies and are therefore sensitive to the electron temperature of the gas.

The T_e calculations were performed in PyNeb. While this requires an input of the electron density (n_e), both the optical and UV [O III] emission lines essentially have no dependence on n_e across the typical range found in H II regions, since their critical densities for collisional de-excitation are $\gg +1000$ cm^{-3}. For this work we adopt n_e values derived from the [S II] λλ 6731/6716 line ratio, which yields $n_e = 158$, 189, 184 cm-3 for SB 2, SB 82, and SB 182, respectively (Table 1).

We consider the possibility that the choice of atomic data may influence the measurements of T_e. This can in turn affect determinations of t^2 and T_0 (see Section 4.1), as well as abundances measured using the T_e method. As such, measurements for T_e and the t^2 analysis presented in this work were run using three different collisional strength data sets for O^{++} (Aggarwal & Keenan 1999; Tayal & Zatsarinny 2017; Mao, Badnell, & Del Zanna 2021). We note that Mao et al. (2021) produced higher values for individual $T_{e\,4363}$ and $T_{e\,1666}$ measurements, but remain consistent within the uncertainties of the results obtained when adopting other collisional datasets. Additionally, the *difference* between the two quantities was the same as those from other data sets, and as such, values for t^2 were not affected by the high individual temperature measurements. We conclude that the choice of atomic data does not significantly affect t^2 results and adopt Tayal & Zatsarinny (2017) collisional strengths throughout this analysis.

The derived $T_{e\,4363}$ and $T_{e\,1666}$ are reported in Table 3. Figure 5 compares their relation with similar measurements by (Mingozzi et al. 2022, hereafter M22), who found rough agreement between the two values. Our results produce a similar distribution along the 1:1 line. Although our sample contains only three galaxies, our measurements have smaller scatter about the 1:1 line compared to M22. Our T_e measurements have a standard deviation scatter of 515 K and a mean absolute percent offset of 4.2%, while the points from M22 have a standard deviation scatter of 1 557 K and a 9.2% mean absolute percent offset. While this smaller scatter may arise in part from the small-sample statistics, or the narrower dynamic range of our sample properties, at face value it suggests that using He II emission lines for reddening and aperture corrections between the UV and optical provides more precise results.

3.4. Ionic oxygen abundance

Using the T_e values calculated above and reported in Table 3, we can derive the O^{++}/H$^+$ abundance for each object by comparing the flux of [O III] and H I lines (namely [O III] λ4959/Hβ which gives the most precise result). In this work, we provide three sets of oxygen abundances in the form of $12 + log(\mathrm{O}^{++}/\mathrm{H}^+)$. The 'UV abundance' is derived using the dust-corrected [O III] λ4959/Hβ ratio with $T_{e\,1666}$. The optical abundance is from the

Table 4. Ion abundances 12+log(O^{++}/H^{+}) measured from [O III] λ4959/Hβ using different T_e values. In the absence of temperature fluctuations, we would expect $T_{e\,4363} = T_{e\,1666} = T_0$, with the results reflecting the true abundance for the region. Temperature fluctuations result in the abundance being higher for the T_0 case. Results where the T_0 abundance is lower are formally unphysical (corresponding to a negative variance in temperature).

	$12+\log(\mathrm{O}^{++}/\mathrm{H}^{+})$		
Object	$T_{e\,4363}$	$T_{e\,1666}$	T_0
SB2	7.68 ± 0.03	7.73 ± 0.02	7.57 ± 0.14
SB82	7.87 ± 0.03	7.85 ± 0.03	7.95 ± 0.21
SB182	7.93 ± 0.02	8.01 ± 0.05	7.79 ± 0.17

Table 5. Emissivity coefficients A_i, B_i, and C_i for each transition.

Transition (i)	A_i	B_i (K)	C_i (erg s^{-1}K$^{-A_i}$ cm^{-3})
[O III] λ1666	0.4	86 351	222 301
[O III] λ4363	0.4	63 417	22 048
[O III] λ4959	0.4	30 115	801.04

Notes: Coefficients were found assuming $n_e = 177$ cm^{-3} (average electron density of the three objects used in this work; see Section 3.3). We note that the C_i obtained are listed here but are not used directly in analysis, as the C_i values for each transition cancel with one another in the final relationship as expressed in Equations (4) and (6).

[O III] λ4959/Hβ ratio using $T_{e\,4363}$, equivalent to the classical direct-T_e method performed with optical spectra. For our sample, the optical and UV metallicities agree with each other to within 0.1 dex. This is a direct result of a nearly 1-to-1 ratio in the $T_{e,1666}$ vs. $T_{e,4363}$ relation (Figure 5). We additionally report third set of $12 + \log(\mathrm{O}^{++}/\mathrm{H}^{+})$ values considering the effect of temperature fluctuations (see Section 4.1 for details). The results of all three methods are provided in Table 4.

4. Discussion

4.1. Temperature fluctuations

Since the UV O III] λλ1661, 1666 and the optical [O III] λ4959 and 4363 lines have different sensitivity to T_e, the discrepancy between the measured T_e in these lines can in principle be used to determine the temperature fluctuations.

We follow the formalism of Peimbert (1967) to derive the strength of temperature fluctuations. In this framework, the temperature structure of a gaseous nebula can be characterised by two parameters: the average temperature T_0 and the dimensionless root mean square temperature fluctuation t^2, where t^2 is then the temperature variance (Peimbert & Peimbert 2013):

$$T_0(\mathrm{O}^{++}) = \frac{\int T_e n_e n(\mathrm{O}^{++}) dV}{\int n_e n(\mathrm{O}^{++}) dV}, \tag{3a}$$

$$t^2(\mathrm{O}^{++}) = \frac{\int (T_e - T_0(\mathrm{O}^{++}))^2 n_e n(\mathrm{O}^{++}) dV}{T_0(\mathrm{O}^{++})^2 \int n_e n(\mathrm{O}^{++}) dV}. \tag{3b}$$

For a single ion (in this case O^{++}), the T_0 and t^2 can be derived from two independent measurements of T_e. Essentially, transitions from higher energy levels (e.g. O III] λ1666 compared to [O III] λ4363) are biased toward higher temperatures, resulting in higher T_e derived using the standard approach (i.e. $T_{e\,1666} > T_{e\,4363}$ when $t^2 > 0$). This difference in derived T_e increases with t^2. Assuming that the level of temperature fluctuations is relatively small compared to the average temperature T_0 (i.e. $t^2 \ll 1$), the measured electron temperatures can be Taylor expanded around the T_0, and the relationship between t^2, T_0 and T_e can be expressed as

$$T_{e,(\lambda1/\lambda2)} = T_0 \left[1 + T_0 \left(\frac{\frac{\varepsilon''_{\lambda1}(T_0)}{\varepsilon_{\lambda1}(T_0)} - \frac{\varepsilon''_{\lambda2}(T_0)}{\varepsilon_{\lambda2}(T_0)}}{\frac{\varepsilon'_{\lambda1}(T_0)}{\varepsilon_{\lambda1}(T_0)} - \frac{\varepsilon'_{\lambda2}(T_0)}{\varepsilon_{\lambda2}(T_0)}} \right) \frac{t^2}{2} \right] \tag{4}$$

as derived by Peimbert & Peimbert (2013). Here $T_{e,(\lambda1\,/\,\lambda2)}$ represents the electron temperature measured from the flux ratio of two emission lines, λ1 and λ2. The quantity $\varepsilon_{\lambda1}(T_0)$ is the emissivity of λ1 at temperature T_0. ε'_i and ε''_i represent the first and second derivatives of ε as a function of T_e.

For collisionally excited lines, the emissivity as a function of T_e can be approximated as

$$\varepsilon_\lambda(T_e) = C_\lambda T_e^{-A_\lambda} \exp(-B_\lambda/T_e)\,, \tag{5}$$

where A_λ, B_λ and C_λ are coefficients for the emission line represented by λ (Osterbrock & Ferland 2006). We find the coefficients for each line of interest by fitting Equation (5) to the emissivity curve derived from PyNeb within the range $T_e = 5\,000$–$20\,000$ K with $n_e = 177$ cm^{-3} (i.e. the average n_e found in Section 3.3). The value of n_e has negligible effect given the high critical densities of the relevant lines. For the O^{++} lines of interest in this work, we find that $A_\lambda = 0.4$ provides an adequate approximation and adopt this as a fixed parameter. The assumed A_λ and best-fit B_λ and C_λ are listed in Table 5. The fitted functions reproduce the emissivities from PyNeb within 2%.

With the coefficients in Table 5, we apply Equations (4) and (5) with the measured values of $T_{e\,1666}$ and $T_{e\,4363}$ from our targets. The dimensionless variance t^2 is directly proportional to the discrepancy between these two temperatures, and can be expressed as

$$t^2\,(T_{e\,4363}, T_{e\,1666}) = \frac{2}{B_{4363} - B_{1666}}[T_{e\,4363} - T_{e\,1666}]. \tag{7}$$

The derived values of t^2 and T_0 are presented in Table 3. Due to the correlation between derived T_0 and t^2, we use the Markov Chain Monte Carlo (MCMC) method to estimate the uncertainties associated with t^2 and T_0. We simultaneously account for systematic uncertainties arising from flux calibration and attenuation correction described earlier. Our MCMC analysis is constructed to fit the observed [O III] λ4959, [O III] λ4363, and O III] λ1666 fluxes. The free parameters are T_0, t^2, and a flux normalisation factor (e.g. relative to He II emission). The $E(B-V)$ values and errors derived from H I Balmer and Paschen lines (see Section 3.2.1) are included as priors to model the optical [O III] λ4959 and [O III] λ4363 fluxes. For UV O III] λ1666 emission, the error budget is dominated by the reliability of using He II flux ratios to correct the aperture and reddening effects. This uncertainty is estimated by adding a ±4 000 K uncertainty in T_e(He II) when predicting the intrinsic He II λ1640/He II λ4686 ratio to derive the reddening- and aperture-corrected O III] λ1666 flux (see Section 3.2.2 for details). The posterior 1σ and 2σ confidence intervals for (t^2, T_0) for SB 2, SB 82, and SB 182 are presented in Figure 6. The 1σ uncertainties in t^2 and T_0 are given in Table 3.

Physically we expect $t^2 \geq\ 0$ due to temperature fluctuations, which result in measured $T_{e\,1666} > T_{e\,4363}$. Surprisingly, however, we find the opposite result for SB 2 and SB 182 with derived $t^2 < 0$. Only SB 82 has a best-fit solution which is physically allowed, but is 1σ consistent with $t^2 = 0$. Our analysis formalism intentionally enables us to derive negative (i.e. unphysical) t^2 values, in order to assess uncertainties and obtain accurate sample averages. As a point of comparison, in Figure 7 we plot t^2 derived

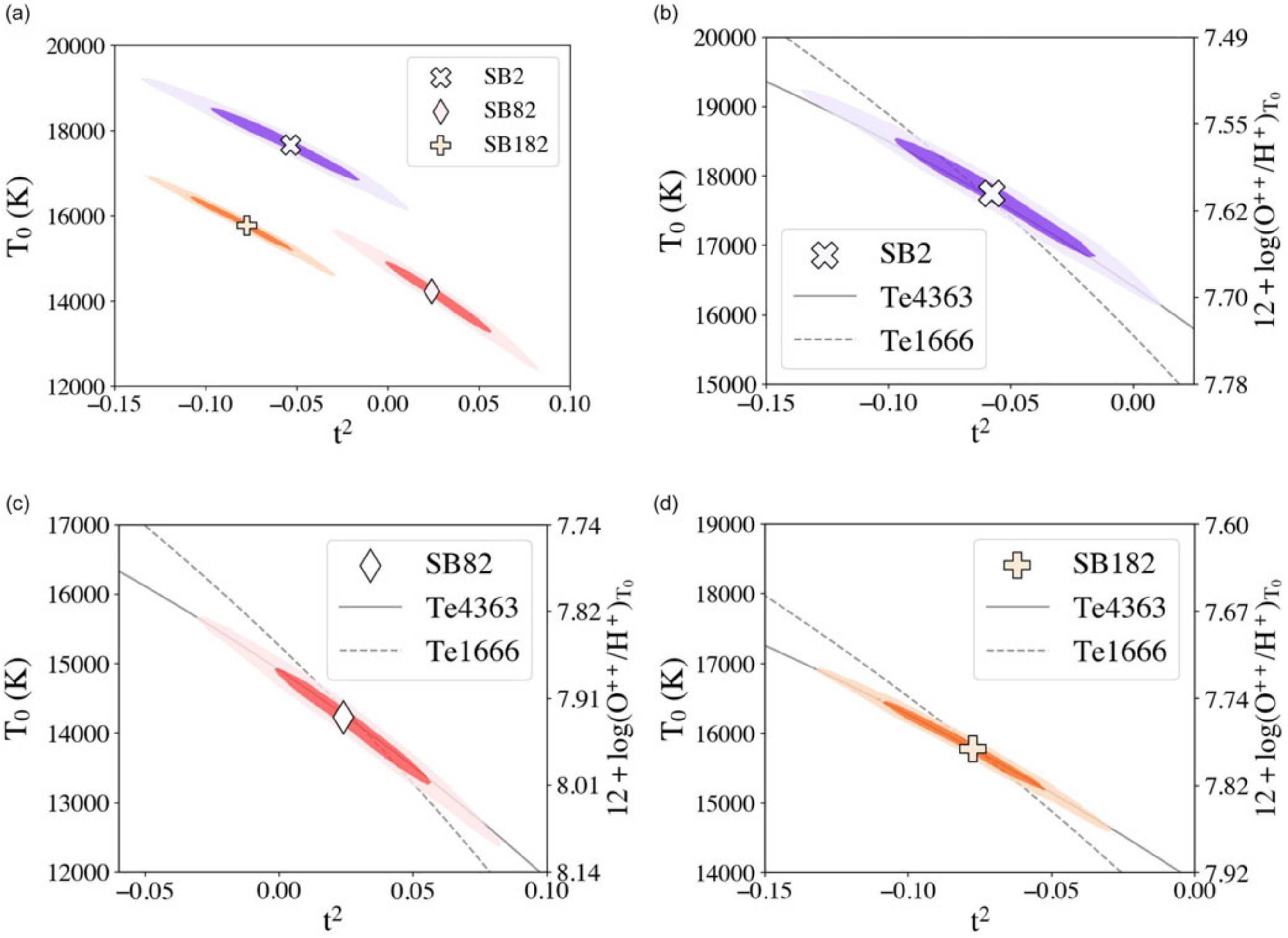

Figure 6. The posterior of T_0 vs. t^2 from the MCMC analysis for the three BCDs in our sample. Panel (a) shows the three BCDs together, denoted by different colours and symbols. The shaded regions indicate the 1σ and 2σ confidence intervals. Panels (b)–(d) zoom in on the individual objects. For each object, the secondary *y*-axis shows the $12 + \log_{10}(\mathrm{O}^{++}/\mathrm{H}^{+})$ abundance at the corresponding T_0. The solid and dashed lines represent the relation between T_0 and t^2 from a single $T_{e,4363}$ or $T_{e,1666}$. We note that the relationship between T_e and t^2 (Equation 6), as derived from Equation (4), is the mathematical reason for the negative value for t^2. However, it is not physically possible for $T_{e\,1666}$ to be less than $T_{e\,4363}$ in the presence of temperature fluctuations.

directly from our sample's T_e measurements with that inferred for a broader literature sample based on the abundance discrepancy factor (i.e. the t^2 needed to reconcile abundances measured from optical CELs and recombination lines). If temperature fluctuations are the dominant cause of the abundance discrepancy, we expect these two methods of obtaining t^2 to agree within the uncertainties. This is clearly not the case for SB 2 and SB 182, which differ by several standard deviations from the typical values $t^2 \approx 0.02$–0.1 inferred from ADF measurements, although SB 82 is in reasonable agreement. Our sample of three targets has an unweighted mean $\langle t^2 \rangle = -0.04 \pm 0.03$ (with sample standard deviation 0.05, larger than the measurement uncertainties). Notably the precision in t^2 measured with our method is comparable to that from ADF-based results. From the results shown in Figure 7, we conclude that our direct measurements of t^2 are generally inconsistent with the values needed to explain the ADF observed in H II regions of similar metallicity.

While our results are in tension with the standard explanation of t^2 as the cause of the ADF, they are consistent with the trend of UV- and optical-based temperatures found by M22. Specifically M22 measured both $T_{e\,4363}$ and $T_{e\,1666}$, and found that they lie approximately on a 1:1 trend. Our measurements fall well within the scatter of the M22 results, as shown in Figure 5. Two of the objects studied in this work, SB 2 and SB 182, were also analysed in M22 and are those for which we report negative values of t^2. For these two objects, our electron temperature measurements are consistent within 1σ of those reported in M22. When accounting for all three objects in this work, our results show a tighter correlation to the 1:1 line than M22's distribution, potentially due to the difference in how the UV dust attenuation is accounted for. The lower scatter using the He II method is promising, and we suggest further analysis involving a larger sample of BCDs with optical and UV He II emission to explore the potential of the He II method as a calibration tool in optical+UV emission line analyses.

As they stand, our t^2 results do not support the temperature fluctuation framework as the physical driver behind the ADF, and an alternate explanation is therefore needed. A key result is that SB 2 and SB 182 exhibit $T_{e\,1666}$ measurements which are *lower* than $T_{e\,4363}$ – an unphysical phenomenon. Effects such as those described by the κ distribution (e.g. Nicholls, Dopita, &

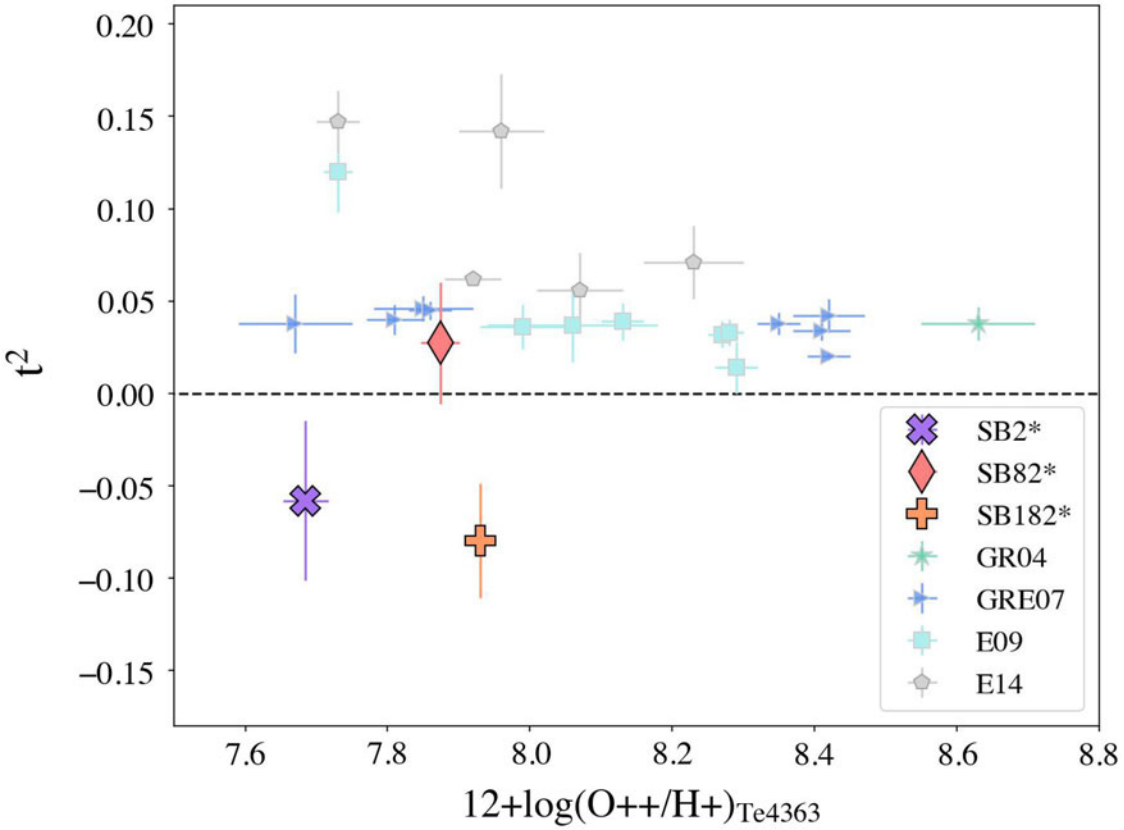

Figure 7. Temperature variance (t^2) and the corresponding O^{++}/H abundances based on $T_{e\,4363}$ for objects SB 2, SB 82, and SB 182 ($*$ = this work), compared to t^2 and O^{++}/H abundances from the literature (García-Rojas et al. 2004; García-Rojas & Esteban 2007; Esteban et al. 2009; Esteban et al. 2014). SB 82 displays a positive t^2 value within 1σ of zero, while our t^2 results for SB 2 and SB 182 are negative. Formally, a negative value for t^2 is unphysical, as this would indicate that UV emission is less affected than optical emission at higher temperatures. However, in the temperature fluctuation paradigm, a negative t^2 is mathematically possible when the measured value for $T_{e\,1666}$ is lower than that of $T_{e\,4363}$. The t^2 values measured directly for our sample are negative on average, and in tension with those inferred to explain the abundance discrepancy factor in the literature sample.

Sutherland 2012) or the multi-component thermal electron distribution model (Storey & Sochi 2014) can be ruled out, since both would enhance the population of all high-energy levels rather than exclusively the 5.35 eV level. An alternate explanation for the ADF is the metal-rich inclusion hypothesis (e.g. Liu et al. 2000; Tsamis et al. 2003; Stasińska et al. 2007). In this scenario, small-scale metal-rich droplets are interspersed throughout the H II region. However, since the droplets are proposed to be cooler and would have essentially no contribution to optical and UV CEL emission lines, including the [O III] λ4363 and O III] λ1666 emission that are being tested in this work, our test does not provide sufficient constraints on this scenario.

In the next section, we further examine the reliability of our analysis and discuss the implications of the unphysical t^2 results for SB 2 and SB 182.

4.2. *Examination of unphysical t^2 results*

We now consider possible effects which could cause the unphysical $t^2 < 0$ values measured for two of the three targets in our sample. H II regions have inherently complex structure, and various physical effects can affect the measurements presented in this work. Temperature fluctuations should lead to derived $T_{e\,1666} \geq T_{e\,4363}$ (corresponding to $t^2 \geq 0$; Equation 6). Our finding of $t^2 < 0$ suggests that some other process may be reducing the observed flux ratio of O III] λ1666/He II 1640 used to derive $T_{e\,1666}$ (or alternatively, increasing the optical [O III]/He II 4686 ratios). In particular, the flux ratio O III] λ1666/He II 1640 would need to increase by ≃10% for SB 2 and SB 182 in order to obtain a result of $t^2 = 0$. Here we examine the extent to which different spatial distributions of [O III] and He II emission regions, combined with differential dust attenuation or aperture effects, can impact the results.

We first consider the effects of differential dust obscuration. UV emission is especially sensitive to dust attenuation. Chen et al. (2024) found that ∼ 50% of the optical [O III] emission could be missing compared to the far-IR [O III] fine-structure emission. A similar mechanism may preferentially occlude O III] λ1666 relative to He II. Since O^{++} and He^{++} are not strictly co-spatial due to having different ionisation energies (35 eV vs. 54 eV), it is possible that the O III] λ1666 and He II λ1640 lines have different attenuation as well. We assess the degree of differential attenuation by comparing optical diagnostics arising from different ionisation zones. In addition to the H I Balmer and Paschen lines reported in Table 2, we also detect He I recombination lines in all targets as well as the optical He II line He II 5411 in SB 2. For SB 2, we derive $E(B-V) = 0.148 \pm 0.021$ from He I 6678/He I 5876, which is considered one of the most robust He I line ratios (Méndez-Delgado et al. 2024), and 0.25 ± 0.11 from He II 5411/He II 4686, compared with 0.167 ± 0.017 from H I. These are consistent within 1σ, with no evidence for less attenuation of He II, though we note the increased uncertainty for $E(B-V)$ measured using He II. For SB

182 we derive $E(B-V)$ 0.009 ± 0.015 from He I 5876/He I 6678, in agreement with the value 0.001 ± 0.012 from H I. We find similar consistency for SB 82, with $E(B-V)$ 0.042 ± 0.018 from He I and 0.035 ± 0.016 from H I, although we note that this object does not have unphysical results. We can also estimate the reddening in the [O III]-emitting zone by using the nearly uniform intrinsic flux ratio of [Ne III] 3869/[O III] 5007 = 0.082, with intrinsic scatter of only 0.04 dex (Jones, Martin, & Cooper 2015). In all cases the observed [Ne III]/[O III] is consistent with that expected from the H I-based reddening. Moreover, multiple diagnostics indicate that the reddening is relatively low in all targets. We conclude that there is no evidence for differential dust attenuation which could cause increased reddening of the [O III] relative to He II emission, and that differential dust attenuation is not responsible for the unphysical t^2 measurements in SB 2 or SB 182.

We now consider whether different spectroscopic apertures, in combination with spatial structure of the targets, could cause the derived negative t^2 values in SB 2 and SB 182. This would require a scenario where the physical region probed by COS in the UV is characterised by an O III] λ1666/He II flux ratio which is ∼10% lower than the region covered by ESI optical spectroscopy (specifically, <10% lower for SB 2 and 13% lower for SB 182). We note that He II emission morphology is often more compact and closer to the ionising source compared to typical nebular emission from [O III] (e.g. Kehrig et al. 2018; Martin, Peng, & Li 2024; Rickards Vaught, Sandstrom, & Hunt 2021). For COS spectra, spatial extent in the dispersion direction can result in broader emission line profiles. We thus checked the spectral FWHM of He II λ1640 and O III] λ1666, and found that He II λ1640 is marginally broader than O III] λ1666 in all three objects (8% broader in SB 2 and SB 182, and 37% broader in SB 82), which may arise from intrinsic kinematic differences or alternatively a larger spatial extent of He II λ1640 that may be possible with strong Wolf-Rayet stellar winds. To more directly quantify the magnitude of aperture effects, we extract the COS spectra using different 'BOXCAR' extraction heights. We consider a 10-pixel height which is similar to the 1.0″ wide ESI slit, and a 35-pixel height which captures all light in the 2.5″ COS aperture. The 35 pixel height is expected to be similar to the TWOZONE extraction used for our primary results, and indeed in all cases they are consistent within the 1σ measurement uncertainties. For SB 2, we find that a 10 pixel BOXCAR extraction height results in an 11% larger O III] λ1666/He II 1640 ratio compared to the TWOZONE extraction, yielding $t^2 = -0.02 \pm 0.02$. For SB 82 and SB 182, all extraction heights yield O III] λ1666/He II 1640 ratios which are consistent within the 1σ uncertainties (<5% and <3% difference, respectively). We find that SB 2 is consistent at the 1σ level with the case of uniform temperature ($t^2 = 0$) when considering possible aperture effects, while the negative t^2 result for SB 182 is not explained by aperture effects. We caution that this analysis of COS aperture effects is subject to complications arising from vignetting and other optical properties (e.g. James et al. 2022). However, the targets in this work are relatively compact such that we expect vignetting and light leakage beyond the nominal 1.25″ COS aperture to be minimal. Ultimately, future integral field spectroscopic observations at both UV and optical wavelengths will be ideal to provide robust aperture matching to resolve this possible issue.

In summary, we investigated whether dust attenuation and aperture effects can plausibly explain the unphysical temperature structure measured for our targets SB 2 and SB 182 (i.e. $T_{e\,1666} < T_{e\,4363}$, and $t^2 < 0$ in our formalism). For SB 2, correcting for aperture effects can bring our measurement within 1σ of $t^2 = 0$, although we still formally find a negative t^2. We find no plausible explanation for SB 182, which shows no significant spatial variations and has reddening consistent with zero. We likewise find no significant change for SB 82 where we derive a slightly positive t^2. Considering these possible systematic uncertainties, we still find an average $t^2 \lesssim 0$ for our aggregate sample which suggests little or no temperature fluctuations.

4.3. Implications and future prospects

Our results show generally good agreement (<0.1 dex) between the T_e and metallicity measured from the optical and UV CELs for O^{++}. This is promising for observations at cosmic dawn ($z \gtrsim 6$), as recent observations of such high-z galaxies from JWST rely on rest-UV nebular emission features to probe their physical properties (e.g. Rhoads et al. 2023; Arellano-Córdova et al. 2022; Jones et al. 2023; Wang et al. 2024; Cameron et al. 2023; Topping et al. 2024; Topping et al. 2022; Leethochawalit et al. 2022). At least for local BCD, our results show that the [O III] emission lines between the optical and UV are consistent with each other within 550 K (∼3.5%) on average. Additionally, our results are consistent with the findings of Bresolin et al. (2016), who found that for low-metallicity systems, T_e-based abundances are in relatively good agreement with the stellar metallicities of young B supergiants accounting for a ∼ 0.1 dex correction to nebular oxygen abundance due to dust depletion.

With continuous spectral coverage from the rest UV to rest optical of galaxies at $z \sim 5$–9, JWST/NIRSpec also offers a unique opportunity to reduce the aperture matching uncertainties and to investigate the reliability of using He II emitting galaxies for similar analyses in the future. Our work using He II to calibrate optical and UV spectra shows that the He II method has potential for increasing the precision of H II region gas-phase diagnostics. We additionally note that in measurements of t^2, the posteriors in the distribution follow $T_{e\,4363}$ (see Figure 6), with the error budget in t^2 being dominated by the error on $T_{e\,1666}$. The error on $T_{e\,1666}$ is largely systematic (arising from the He II correction of the UV oxygen lines), which indicates a promising prospect for future observations as future targets may not need such high SNR as the objects presented in this work. More comparisons, especially at various redshifts, would collectively yield stronger constraints on t^2 and the systematic uncertainties.

In addition to the traditional 1D spectral analysis, recent observations using integral field units (IFU) have proven to be valuable in determining the spatial structure of ionised nebulae, especially the spatial extent of different ions (e.g. Kehrig et al. 2018; McLeod et al. 2019; Kumari, James, & Irwin 2017; Westmoquette et al. 2007; Fensch et al. 2016; Lago et al. 2019; Weilbacher et al. 2015; Cosens et al. 2022). Similar observations focusing on He II emitting galaxies would help us determine the systematic bias of our method. We additionally note that the three objects studied in this work do not have a measured ADF as we do not have measurements of their oxygen RLs. Knowing the magnitude of the ADF is not strictly necessary for determining the magnitude of temperature fluctuations or making direct T_e measurements, but would certainly aid with interpreting the results. Having a known ADF would be valuable context for the measured values of t^2, and to test whether our direct measurements of t^2 correlate with those inferred from the ADF. As such, follow up to obtain RLs and to measure the ADF (or lack thereof) in SB 2, SB 82, and SB 182 would be a natural next step in order to better understand the physical driver behind the ADF.

5. Summary

In this work, we present a novel method that uses the nebular He II λ1640 and He II λ4686 emission lines to perform aperture and reddening correction between UV (HST/COS) and optical (Keck/ESI) spectra, facilitating precise direct comparisons for O^{++}/H^{+} abundances and T_e measured between the optical and UV for three nearby BCDs. Our main findings are:

- UV and optical T_e are consistent with each other within ~ 500 K (standard deviation of scatter). This result is consistent with the similar analysis by M22 using SED models for aperture matching, but appears to be closer to the 1-to-1 ratio and exhibits smaller scatter, indicating that our method could improve the precision in matching the UV- and optical-based nebular properties for similar galaxies.
- Similarly, the UV and optical O^{++}/H^{+} metallicities are consistent with each other within 0.1 dex, verifying that for local dwarf galaxies, the gas-phase metallicities measured between the UV and optical CEL methods can be used interchangeably, and that UV CELs can be reliably used to trace oxygen abundances using the T_e method.
- Two galaxies (SB 2 and SB 182) have $T_{e\,1666} < T_{e\,4363}$, and UV-based 12+log($O^{++}/H^{+}$) which is larger than the optical-based value, an unphysical result which contradicts predictions from temperature fluctuation scenarios which are often invoked to explain the abundance discrepancy factor. The unphysical t^2 value for SB 2 can be attributed in part to possible aperture effects. For SB 182, the physical cause behind the unphysical t^2 value remains an open question.

This work successfully validates the feasibility of using nebular He II emission to match the UV and optical spectra observed from different instruments. However, with only three galaxies in the sample, this work is subject to small-sample statistical uncertainties and sample variance. Similar observations of a larger sample of He II emitting galaxies, as well as acquiring ADF measurements for the three objects studied in this work, would significantly improve our understanding of potential systematic uncertainties and help to address the physical cause for objects with derived $t^2 < 0$. Additionally, observations from JWST and optical IFUs on He II emitting galaxies can help to further validate and understand the systematic biases which may be inherent in this methodology. Overall, our results establish a clear foundation for using rest-frame optical and UV emission line diagnostics interchangeably, enabling robust studies of chemical evolution and other galaxy properties based on these features, applicable from the present-day universe to the most distant objects being studied with JWST.

Acknowledgements. This research is based largely on observations with the NASA/ESA Hubble Space Telescope obtained from the Space Telescope Science Institute, which is operated by the Association of Universities for Research in Astronomy, Incorporated, under NASA contract NAS5-26555. These observations are associated with programmes HST-GO-15646 and HST-GO-14168. Support for programme number HST-GO-15646 was provided through a grant from the STScI under NASA contract NAS5-26555. TJ acknowledges support from the NASA under grants HST-GO-15646, HST-GO-16697, and 80NSSC23K1132, and from a UC Davis Chancellor's Fellowship. YC is supported by the Direct Grant for Research (C0010-4053720) from the Faculty of Science, the Chinese University of Hong Kong. The optical spectroscopic data presented herein were obtained at the W. M. Keck Observatory, which is operated as a scientific partnership among the California Institute of Technology, the University of California and the National Aeronautics and Space Administration. The Observatory was made possible by the generous financial support of the W. M. Keck Foundation. The authors wish to recognise and acknowledge the very significant cultural role and reverence that the summit of Mauna Kea has always had within the indigenous Hawaiian community. We are deeply appreciative of the opportunity to conduct observations from this mountain. In addition, EH would like to give special thanks to Kelsey Glazer and Dr. Erika Holmbeck, who made the completion of this work possible.

Data availability statement. The HST/COS spectra used in this article are publicly available at Mikulski Archive for Space Telescopes (MAST) Portal. The raw Keck/ESI observations are available at the Keck Observatory Archive (KOA). The reduced spectra can be shared by the authors upon reasonable request.

References

Aggarwal, K. M., & Keenan, F. P. 1999, ApJS, 123, 311
Andrews, B. H., & Martini, P. 2013, ApJ, 765, 140
Arellano-Córdova, K. Z., et al. 2022, ApJ, 940, L23
Arellano-Córdova, K. Z., et al. 2026, MNRAS, 547, stag380
Berg, D. A., et al. 2022, ApJS, 261, 31
Blanc, G. A., Kewley, L., Vogt, F. P. A., & Dopita, M. A. 2015, ApJ, 798, 99
Bresolin, F., et al. 2016, ApJ, 830, 64
Bresolin, F., Kudritzki, R.-P., Urbaneja, M. A., Sextl, E., & Riess, A. G. 2025, ApJ, 991, 151
Bunker, A. J., et al. 2023, A&A, 677, A88
Calzetti, D., et al. 2000, ApJ, 533, 682
Cameron, A. J., et al. 2023, A&A, 677, A115
Cardelli, J. A., Clayton, G. C., & Mathis, J. S. 1989, ApJ, 345, 245
Chen, Y., et al. 2026, ApJ, 1000, 150
Cosens, M., et al. 2022, in American Astronomical Society Meeting Abstracts, Vol. 240, American Astronomical Society Meeting #240, 333.06D
Croxall, K. V., et al. 2013, ApJ, 777, 96
Cullen, F., Cirasuolo, M., McLure, R. J., Dunlop, J. S., & Bowler, R. A. A. 2014, MNRAS, 440, 2300
Curti, M., Mannucci, F., Cresci, G., & Maiolino, R. 2020, MNRAS, 491, 944
Curti, M., et al. 2023, MNRAS, 518, 425
Curti, M., et al. 2025, A&A, 697, A89
Davé, R., Finlator, K., & Oppenheimer, B. D. 2011, MNRAS, 416, 1354
Davé, R., Rafieferantsoa, M. H., Thompson, R. J., & Hopkins, P. F. 2017, MNRAS, 467, 115
Erb, D. K. 2008, ApJ, 674, 151
Erb, D. K., et al. 2006, ApJ, 644, 813
Esteban, C., et al. 2009, ApJ, 700, 654
Esteban, C., et al. 2014, MNRAS, 443, 624
Fensch, J., Duc, P. A., Weilbacher, P. M., Boquien, M., & Zackrisson, E. 2016, A&A, 585, A79
Froese Fischer, C., & Tachiev, G. 2004, Atomic Data and Nuclear Data Tables, 87, 1
García-Rojas, J., & Esteban, C. 2007, ApJ, 670, 457
García-Rojas, J., et al. 2004, ApJS, 153, 501
Gordon, K. D., Clayton, G. C., Misselt, K. A., Landolt, A. U., & Wolff, M. J. 2003, ApJ, 594, 279
Hayes, M. J., et al. 2025, ApJ, 982, 14
Hsiao, T. Y.-Y., et al. 2025, ApJ, 993, 70
James, B. L., et al. 2022, ApJS, 262, 37
Jones, T., Martin, C., & Cooper, M. C. 2015, ApJ, 813, 126
Jones, T., et al. 2023, ApJ, 951, L17

Kehrig, C., et al. 2011, A&A, 526, A128
Kehrig, C., et al. 2015, ApJ, 801, L28
Kehrig, C., et al. 2018, MNRAS, 480, 1081
Kelly, P. M., et al. 2025, ApJ, 993, 65
Kreckel, K., et al. 2022, A&A, 667, A16
Kriek, M., et al. 2015, ApJS, 218, 15
Kumari, N., James, B. L., & Irwin, M. J. 2017, MNRAS, 470, 4618
Kunth, D., Lequeux, J., Mas-Hesse, J. M., Terlevich, E., & Terlevich, R. 1997, in Revista Mexicana de Astronomia y Astrofisica Conference Series, Vol. 6, ed. J. Franco, R. Terlevich, & A. Serrano, 61
Lago, P. J. A., Costa, R. D. D., Fa′undez-Abans, M., & Maciel, W. J. 2019, MNRAS, 489, 2923
Leethochawalit, N., Trenti, M., Morishita, T., Roberts-Borsani, G., & Treu, T. 2022, MNRAS, 509, 5836
Lilly, S. J., Carollo, C. M., Pipino, A., Renzini, A., & Peng, Y. 2013, ApJ, 772, 119
Liu, X. W., et al. 2000, MNRAS, 312, 585
Luridiana, V., Morisset, C., & Shaw, R. A. 2015, A&A, 573, A42
Maiolino, R., et al. 2008, A&A, 488, 463
Mao, J., Badnell, N. R., & Del Zanna, G. 2021, A&A, 653, A81
Martin, C. L., Peng, Z., & Li, Y. 2024, ApJ, 966, 190
McLeod, A. F., et al. 2019, MNRAS, 486, 5263
Méndez-Delgado, J. E., et al. 2022, MNRAS, 510, 4436
Méndez-Delgado, J. E., et al. 2025, ApJ, 986, 74
Mingozzi, M., et al. 2022, ApJ, 939, 110
Momcheva, I. G., et al. 2016, ApJS, 225, 27
Nakajima, K., et al. 2023, ApJS, 269, 33
Nicholls, D. C., Dopita, M. A., & Sutherland, R. S. 2012, ApJ, 752, 148
Osterbrock, D. E., & Ferland, G. J. 2006, Astrophysics of Gaseous Nebulae and Active Galactic Nuclei, 2nd. ed. by D.E. Osterbrock and G.J. Ferland. Sausalito, CA: University Science Books
Peeples, M. S., & Shankar, F. 2011, MNRAS, 417, 2962
Peimbert, A., & Peimbert, M. 2013, ApJ, 778, 89
Peimbert, M. 1967, ApJ, 150, 825
Rhoads, J. E., et al. 2023, ApJ, 942, L14
Rickards Vaught, R. J., Sandstrom, K. M., & Hunt, L. K. 2021, ApJ, 911, L17
Rickards Vaught, R. J., et al. 2024, ApJ, 966, 130
Sanders, R. L., Shapley, A. E., Topping, M. W., Reddy, N. A., & Brammer, G. B. 2024, ApJ, 962, 24
Sanders, R. L., et al. 2021, ApJ, 914, 19
Sarkar, A., et al. 2025, ApJ, 978, 136
Schaerer, D., & Vacca, W. D. 1998, ApJ, 497, 618
Schaerer, D., Fragos, T., & Izotov, Y. I. 2019, A&A, 622, L10
Schaerer, D., et al. 2022, A&A, 665, L4
Senchyna, P., et al. 2017, MNRAS, 472, 2608
Senchyna, P., et al. 2020, MNRAS, 494, 941
Senchyna, P., et al. 2022, ApJ, 930, 105
Sheinis, A. I., et al. 2002, PASP, 114, 851
Shirazi, M., & Brinchmann, J. 2012, MNRAS, 421, 1043
Stasińska, G., Tenorio-Tagle, G., Rodríguez, M., & Henney, W. J. 2007, A&A, 471, 193
Steidel, C. C., et al. 2014, ApJ, 795, 165
Storey, P. J., & Sochi, T. 2014, MNRAS, 440, 2581
Stott, J. P., et al. 2016, MNRAS, 457, 1888
Tacconi, L. J., et al. 2018, ApJ, 853, 179
Tang, M., et al. 2026, ApJ, 1001, 38
Tayal, S. S., & Zatsarinny, O. 2017, ApJ, 850, 147
Taylor, A. J., Barger, A. J., & Cowie, L. L. 2022, ApJ, 939, L3
Topping, M. W., et al. 2022, ApJ, 941, 153
Topping, M. W., et al. 2024, MNRAS, 529, 4087
Tremonti, C. A., et al. 2004, ApJ, 613, 898
Treu, T., et al. 2015, ApJ, 812, 114
Troncoso, P., et al. 2014, A&A, 563, A58
Trump, J. R., et al. 2023, ApJ, 945, 35
Tsamis, Y. G., Barlow, M. J., Liu, X. W., Danziger, I. J., & Storey, P. J. 2003, MNRAS, 338, 687
Wang, X., et al. 2024, ApJ, 967, L42
Weilbacher, P. M., et al. 2015, A&A, 582, A114
Westmoquette, M. S., Exter, K. M., Smith, L. J., & Gallagher, J. S. 2007, MNRAS, 381, 894
Wisnioski, E., et al. 2015, ApJ, 799, 209
York, D. G., et al. 2000, AJ, 120, 1579